Electronic Supporting Information

Oxygen Vacancy Engineered Unsaturated Coordination in Cobalt Carbonate Hydroxide Nanowires Enables Highly Selective Photocatalytic CO_2 Reduction

Huanhuan Liu, Fu Zhang, Haifei Wang, Jierui Xue, Yiming Guo, Qizhu Qian and Genqiang Zhang*

Hefei National Laboratory for Physical Sciences at the Microscale, CAS Key Laboratory of Materials for Energy Conversion, Department of Materials Science and Engineering, University of Science and Technology of China, Hefei, Anhui 230026, China

* Corresponding Author

E-mail address: gqzhangmse@ustc.edu.cn (G.Q. Zhang)

1. Experimental

1.1 Materials

Cobalt nitrate hexahydrate ($Co(NO_3)_2 \cdot 6H_2O$) and ammonium fluoride (NH_4F) were purchased from Aladdin Industrial Corporation. Urea was purchased from Sinopharm Chemical Reagent Corporation. All of chemical reagents were used in our experimentation without any further purification.

1.2 Synthesis of photocatalysts.

Synthesis of CCO NWs photocatalyst. In a typical synthetic procedure, 300 mg $Co(NO_3)_2 \cdot 6H_2O$, 50 mg NH_4F and 210 mg urea were dissolved in 70 mL of distilled water with the assistance of ultrasonication for 30 min. The mixture was sealed in a 100 mL Teflon-lined stainless-steel autoclave and then placed in an oven at 120 °C for 12 h. The product was collected by centrifugation, washed with distilled water for at least three times, and finally dried in an oven at 70 °C for 12 h.

Synthesis of CCO NWs photocatalyst with oxygen vacancy (Vo). As shown in **Fig. S1**, a self-photoetching approach was carried out in an all glass automatic on-line trace gas analysis system (Labsolar-6A, Beijing Perfectlight Technology Co., Ltd.) connecting to water bath for maintaining the reaction temperature at 25 °C. To generation Vo on the surface of CCO NWs, the 0.1 g as-prepared CCO NWs photocatalyst were dispersed on the bottom of a 150 mL top-irradiation-type Pyrex reaction cell. The air in the cell was evacuated by a vacuum pump before irradiated. The vacuum level was assured by vacuum indicator equipped with all glass automatic on-line trace gas analysis system. The distance between light source and sample is about 11 cm.

The as-prepared CCO photocatalyst was illuminated by a 300 W Xe lamp (PLS-SXE 300, Beijing PerfectLight Co., Ltd. China) under vacuum for some time to obtain different samples. The illuminating time at 3 h, 5 h and 10 h were named as Vo-CCO-3 NWs, Vo-CCO NWs and Vo-CCO-10 NWs.

1.3 Materials characterization:

The morphology of the as-prepared samples were observed by scanning electron microscope (SEM, Hitachi SU8200, Japan) and transmission electron microscopy (TEM, Talox F200X, America). The X-ray diffraction (XRD, TTR-III, Japan) pattern with a Cu Kα source was used to analyze crystalline structures. The chemical state of the as-prepared samples was performed with Fourier transform infrared spectroscopy (FTIR, Nicolet 8700, America) and confocal Raman microscope (LabRam HR, Japan) using a He/Ne laser (532 nm) as the excitation source. The X-ray photoelectron spectroscopy (XPS) were acquired on an ESCALAB MKII with Mg Kα (hυ = 1253.6 eV) as the excitation source. An Ar^+ beam were employed to detect the quantity of oxygen vacancies with a electron energy of 12.5 V, filament current of 3 mA, emission current of 7.5 A and energy of 2 KV. The K-edge X-ray absorption spectroscopy (XAS) of carbon and oxygen and the L-edge XAS of cobalt were measured at the National Synchrotron Radiation Laboratory (NSRL), Hefei, China. The XANES and EXAFS of Co K-edge spectra are collected on the beamline BL01C1 in NSRRC. The obtained XAFS data was processed in Athena (version 0.9.26)[1] for background, pre-edge line and post-edge line calibrations. Then Fourier transformed fitting was carried out in Artemis (version 0.9.26). The k^3-weighting, k-range of 3 - 12 $Å^{-1}$ and R range of 1 - 3 Å were used for the fitting of Co foil; k-range of ~2 - ~9 $Å^{-1}$ and R range of 1 – 3.2 Å were used for the fitting of Co samples. The four parameters,

coordination number, bond length, Debye-Waller factor and E_0 shift (CN, R, σ^2, ΔE_0) were fitted without anyone was fixed, constrained, or correlated. For Wavelet Transform analysis, the χ(k) exported from Athena was imported into the Hama Fortran code. The parameters were listed as follow: R range, 1 - 4 Å, k range, 0 - 13 $Å^{-1}$ for Co foil and 0 - 9 $Å^{-1}$ for Co samples; k weight, 2; and Morlet function with κ=10, σ=1 was used as the wavelet transforms to provide the overall distribution. The optical character of the sample was obtained by UV-Vis diffuse reflectance spectra (UV-Vis DRS, SOLID3700, Japan). The pore structures and surface areas were measured by the Brunauer-Emmett-Teller (BET) N_2 adsorption–desorption isotherms (TriStar II 3020, America). The surface photovoltage spectra (SPV) and were carried out on a homemade apparatus (PL-SPV/IPCE1000 Beijing Perfect light Co., Ltd. China), which consist of a source of monochromatic light with a light chopper (SR 540, Stanford research, Inc.), and a lock-in amplifier. The measurement was performed in air atmosphere and room temperature. The steadystate photoluminescence (PL) spectra were obtained on an F-4600 FL spectrophotometer (Hitachi Ltd, Japan) with an excitation wavelength of 400 nm. Time-resolved PL curves were acquired using a timecorrected single photon counting (TCSPC) system (FM4-TCSPC, Horiba Jobin Yvon) with an excitation wavelength of 470 nm. The electron paramagnetic resonance (EPR) spectra was characterized by JES-FA200 (JEOL, Japan). For in-situ EPR spectra, CCO and Vo-CCO NWs were placed in a paramagnetic tube and then fixed on EPR resonator, respectively. The sample was filled with Ar to eliminate the air in the tube. After that, the paramagnetic tube was sealed by stopper and sealing film. After EPR testing, the Ar was eliminated by CO_2 for about ten minutes. The data are recorded before and after 300 W Xe lamp irradiation, respectively. In-situ FTIR

spectra were acquired by a Thermo Scientific Nicolet iS50 FTIR Spectrometer equipped with a narrowband mercury cadmium telluride (HgCdTe) detector. Typically, 5 mg Vo-CCO NWs powder were pressed into a self-supported plate and placed in the chamber. Before the IR measurement, the air in the chamber was removed by humid CO_2 for 30 min. After that, a 365 nm LED light was used as the light source to drive the photocatalytic reaction. IR spectra were recorded by averaging 32 scans with a resolution of 4 cm^{-1}.

1.4 Electrochemical measurements:

Electrochemical measurements were carried out by a CH Instruments 660E electrochemical workstation in a three electrode cell using platinum wire, fluorine doped tin oxide (FTO) coated with catalysts and Ag/AgCl as the counter electrode, working electrode and reference electrode, respectively. 0.5 M Na_2SO_4 was saturated by Ar or CO_2 as the electrolyte. The details of the working electrodes were described as follows: 5 mg catalyst was dispersed in 1 mL absolute ethanol and 5 uL nafion by sonication. Then, 10 µL of the suspension was drop-coated at FTO glass with an area of 1 × 1 cm^2. The FTO glasses were dried at 80 ^oC for 24 h to remove volatile organic compound before using. A 300 W xenon lamp (PLS-SXE 300, Beijing PerfectLight Co., Ltd. China) was applied as a light source in photocurrent, electrochemical impedance spectrum (EIS) and open circuit potential measurement. A -0.5 V bias potential vs. Ag/AgCl electrode were used in the photocurrent and EIS. Mott-Schottky plots were calculated by an impedance-potential curve with the frequency of 1.0 and 2.0 kHz, respectively. CV curves were performed using a glassy carbon disk as working electrode, a platinum wire as counter electrode and a SEC as reference electrode in CH_3CN containing 0.1 M tetrabutylammonium

hexafluorophosphate ($TBAPF_6$) as a supporting electrolyte under Ar or CO_2 atmosphere, respectively.

1.5 Photocatalytic CO_2 reduction

The photocatalytic experiments were performed in a 450 mL top-irradiation-type Pyrex reaction cell connecting to a water bath for maintaining the reactor temperature of 25 ^oC at atmospheric pressure. Typically, the reaction system containing $[Ru(bpy)_3]Cl_2\cdot$(10 mg, bpy = 2'2-bipyridine), as-prepared photocatalysts (20 mg), and solvent (100 mL, acetonitrile/ H_2O/ triethanolamine, 3/1/1 in volume) was stirred with a magnetic stirrer. A 300 W xenon lamp (PLS-SXE 300, Beijing PerfectLight Co., Ltd. China) equipped with a cutoff filter to filter out the ultraviolet region below 420 nm was supplied as a visible light source (λ > 420 nm) in photocatalytic tests. The system was thoroughly purged with high-pure CO_2 (99.999%) for more than 30 min to dislodge the air in the cell before irradiated. The amounts of CO and H_2 evolved were determined using gas chromatograph (Techcomp GC-7900, China) equipped with a TDX-01 packed column. H_2 was detected using a thermal conductivity detector (TCD). CO was converted by a methanation reactor to CH_4 and then analyzed by a flame ionization detector (FID). The durability of Vo-CCO NWs was investigated with the same procedure described above. After 6 h irradiation, the catalyst was removed from the mixture by supercentrifugation. The catalyst was redisposed in an original solution after drying and weighing by partition strategy.[2] ^{1}H-NMR spectra were recorded on a Bruker Avance III 400 MHz NMR spectrometer. After photocatalytic CO_2 reduction, the catalyst was removed from the mixture by supercentrifugation. 400 uL liquid products and 200 µL D_2O (deuterated water) were mixed in NMR tube. The one-

dimensional ^{1}H spectra was measured with water suppression at 4.7 peak by using a pre-saturation method.

2. Figures

Fig. S1. The reaction equipment of self-photoetching process.

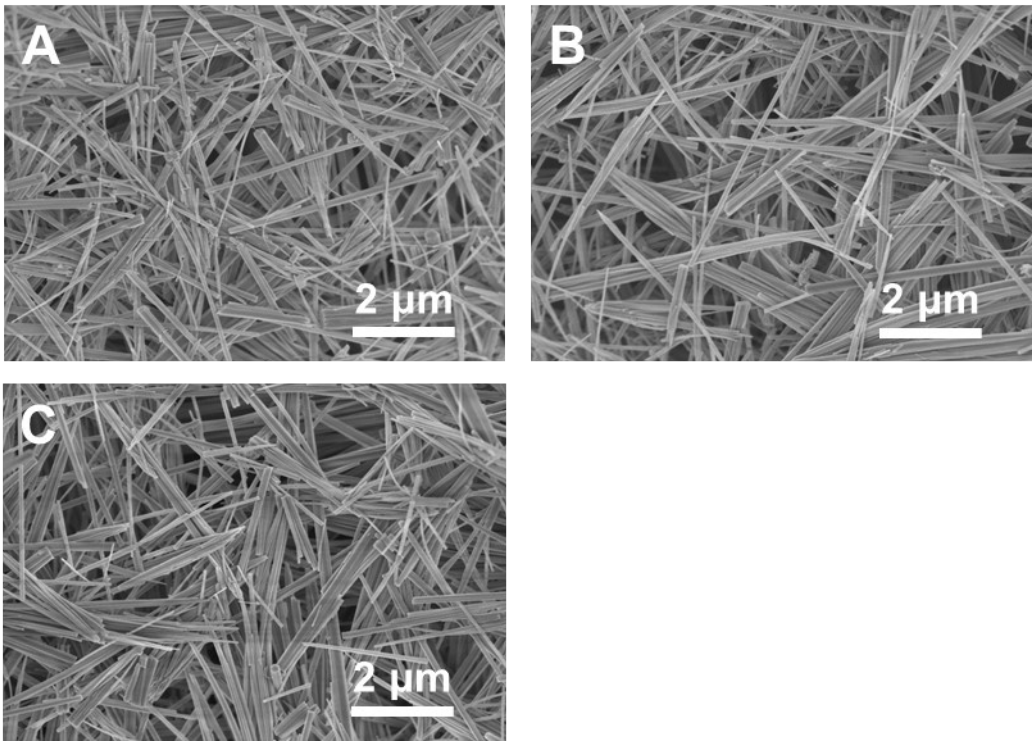

Fig. S2. The SEM of (A) CCO NWs, (B) Vo-CCO-3 NWs and (C) Vo-CCO-10 NWs.

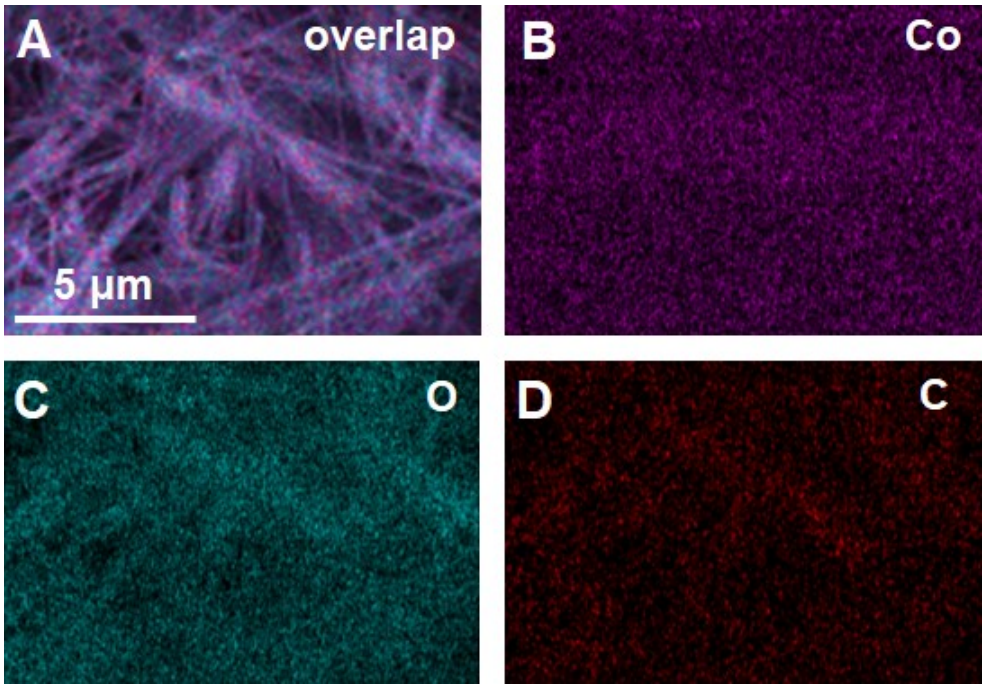

Fig. S3. SEM image elemental mapping of the as-prepared Vo-CCO NWs.

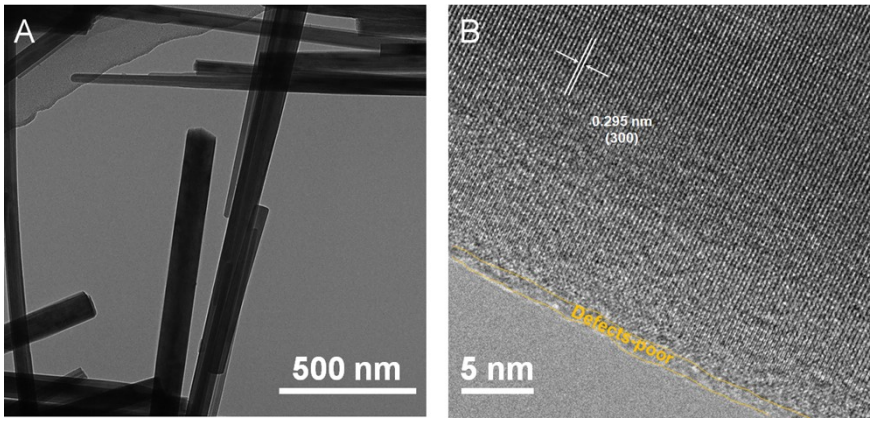

Fig. S4. (A) TEM image and (B) HRTEM image of CCO NWs, respectively.

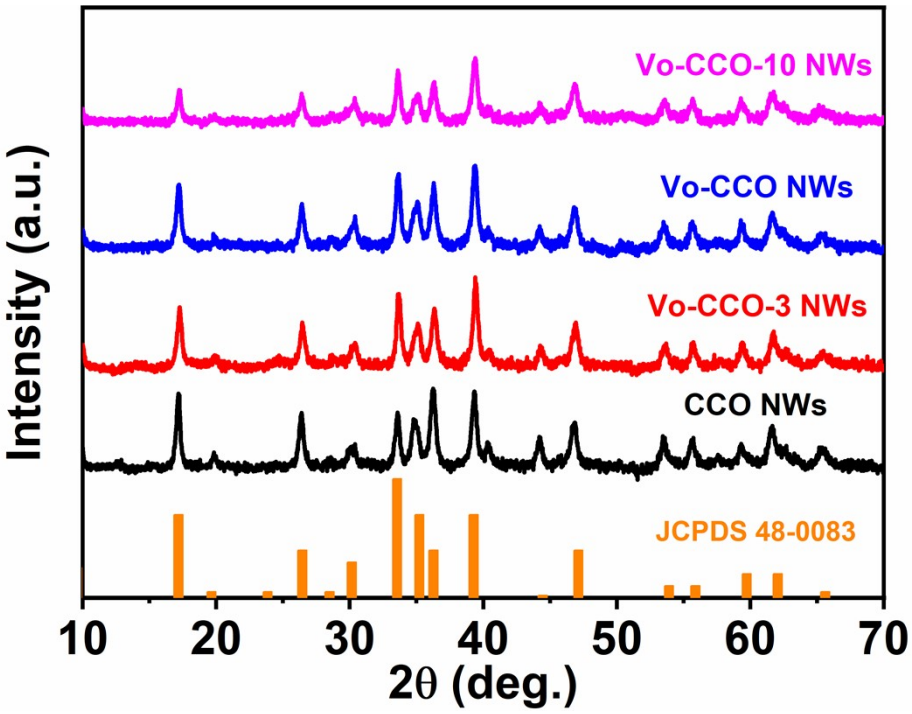

Fig. S5. The XRD patterns of as-prepared different samples.

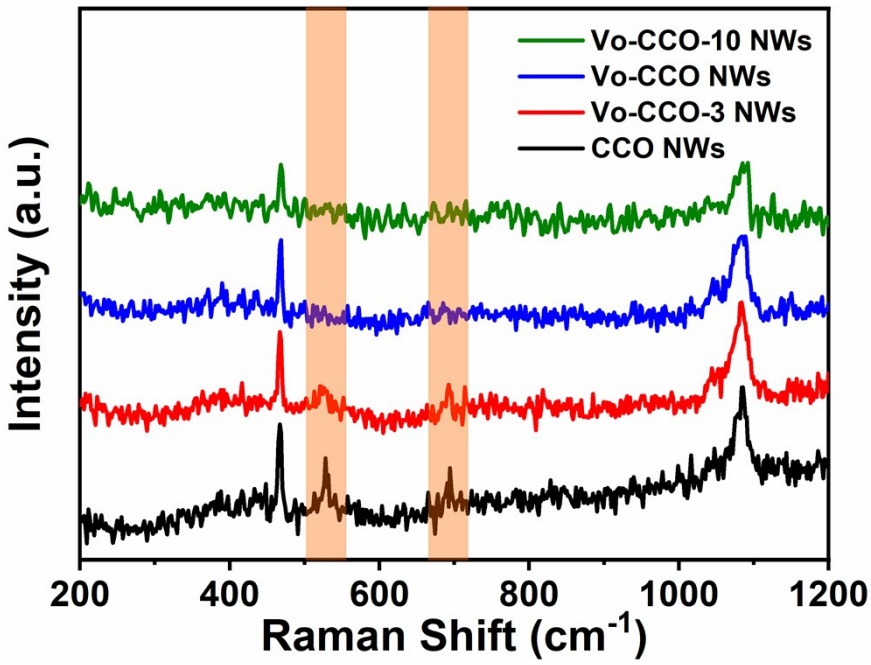

Fig. S6. Raman scattering spectra of as-prepared different samples.

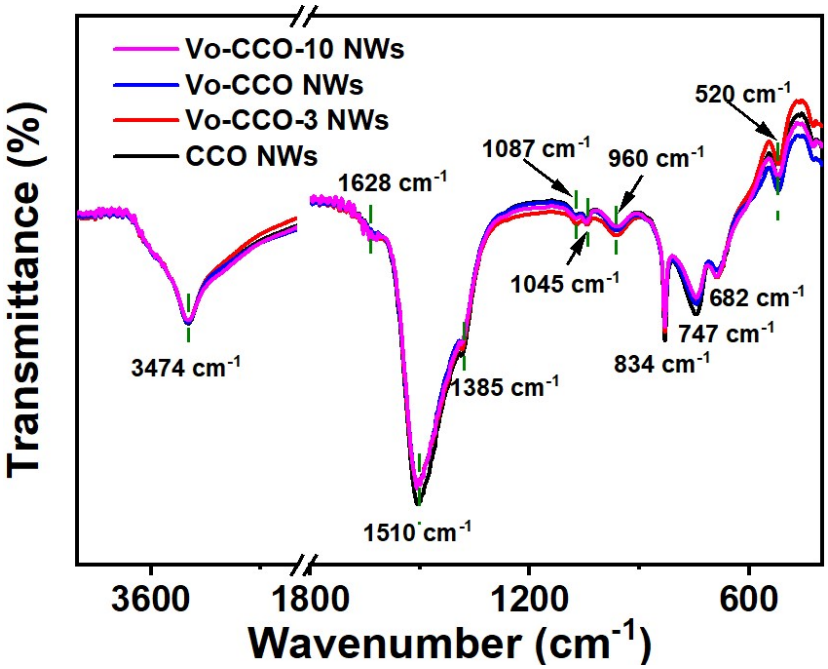

Fig. S7. FTIR spectra of as-prepared different samples.

The peaks center at 3474 and 1628 cm^{-1} are ascribed to O-H group stretching and bending modes of water molecules.[3, 4] The peak at 1510 cm^{-1} can be indexed to stretching vibrations of $\nu(OCO_2)$.[4] The peaks seated at 1087 and 1385 cm^{-1} are identified to the symmetrical and asymmetrical stretching vibration modes of CO_3^{2-}, while the peaks located at 682 and 834 cm^{-1} are assigned to in-plane and out-of-plane bending vibration of CO_3^{2-}. In aaddition, the peak at 747 cm^{-1} is allocated to carbonate species bound via two oxygen centers ($\delta(OCO)$).[3] The peaks at 520 cm^{-1} can be assigned to ρ_w (Co-OH).[4] The peaks at 1510, 834, 747 and 682 cm^{-1} show a significant decrease of Vo-CCO NWs compared with CCO NWs, indicating that cracked chemical bond of Co-O is due to the reduce of carbonate species bond with Co, which is consistent with the result of Raman spectra.

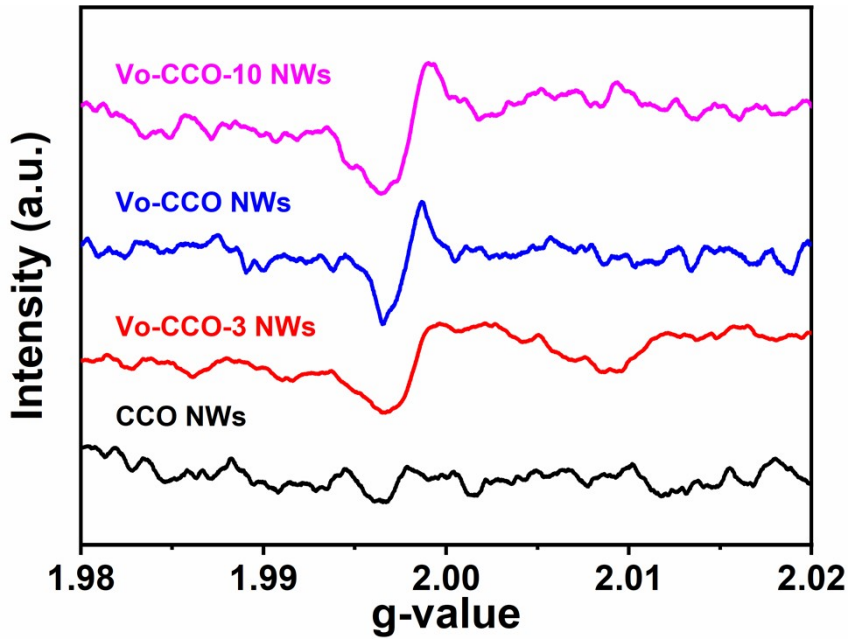

Fig. S8. EPR spectra of as-prepared different samples.

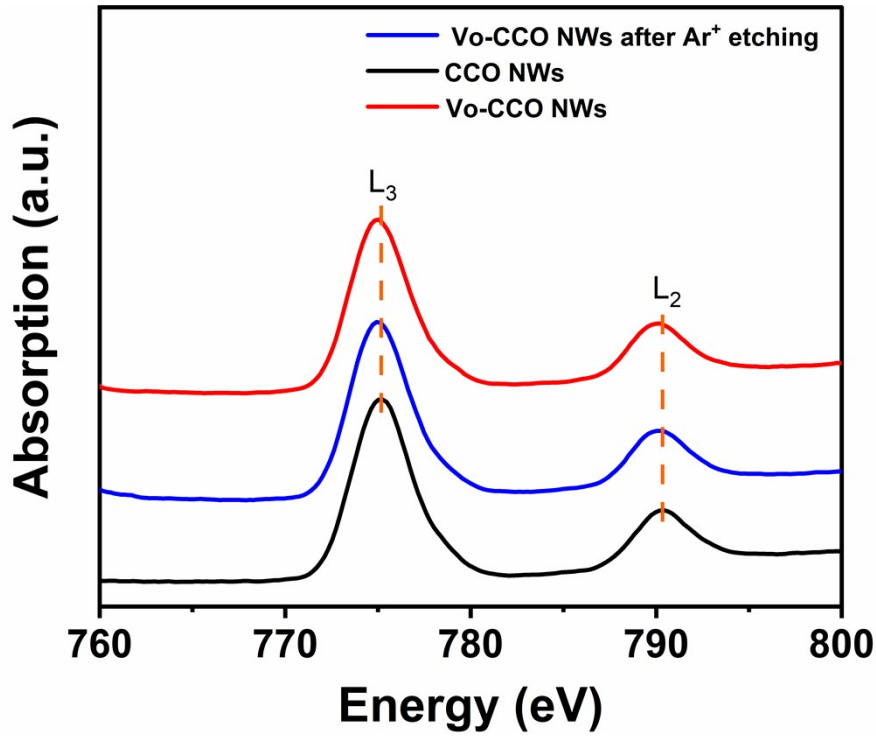

Fig. S9. Co K-edge XAS spectra.

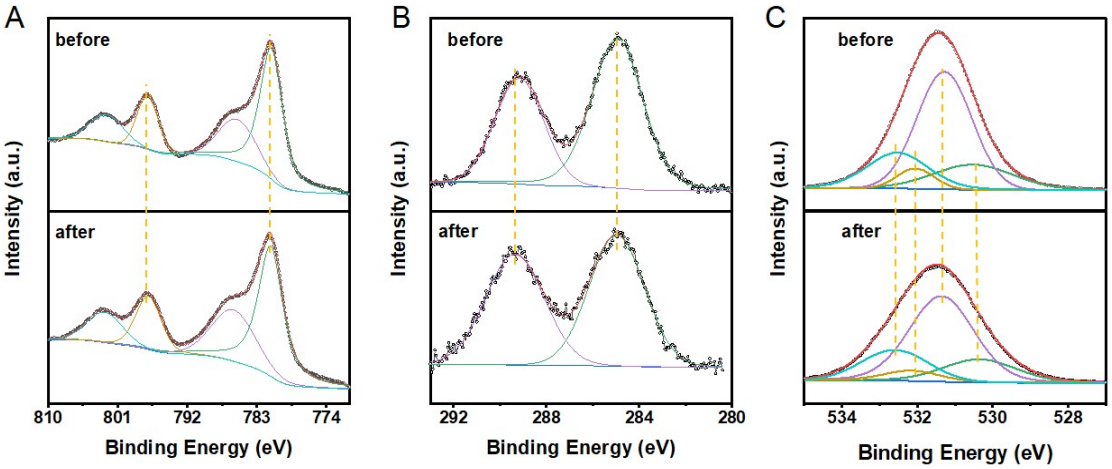

Fig. S10. XPS spectra of CCO NWs before and after Ar^+ etching: (A) Co 2p, (C) C 1s and (C) O 1s.

There is no significant difference before and after Ar^+ etching, indicating the stable structure and consistent chemical composition of CCO NWs.

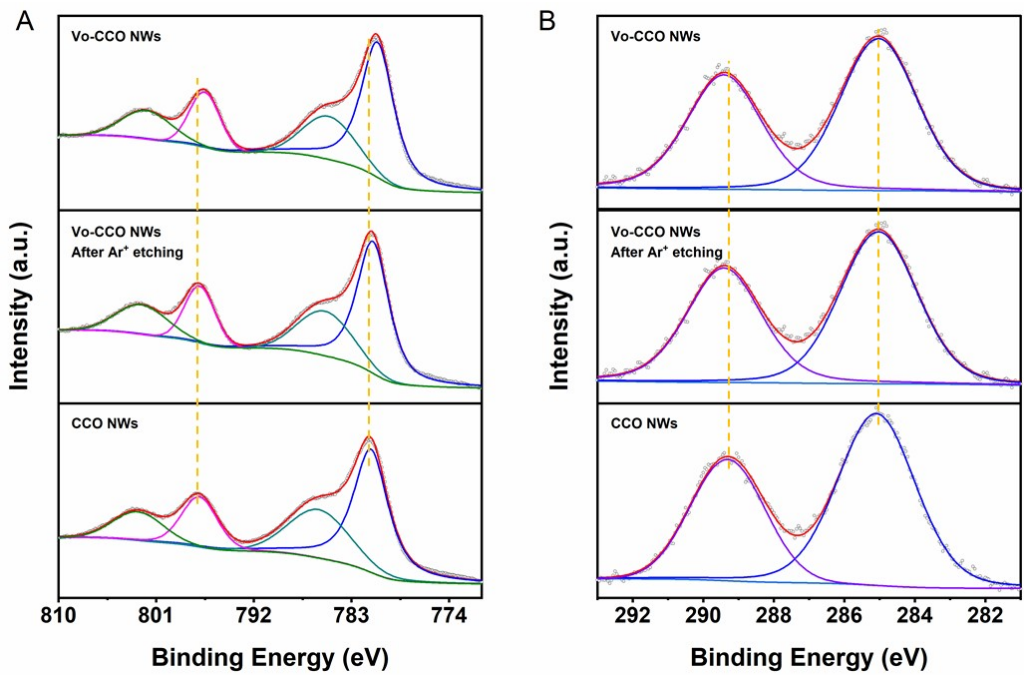

Fig. S11. XPS spectra of CCO and Vo-CCO NWs: (A) Co 2p and (B) C 1s.

The peaks at 797.0 and 781.4 eV of Co 2p XPS spectra (**Fig. S11A**) are attributed to Co $2p_{1/2}$ and $2p_{3/2}$ spin-orbit of Co^{2+}, respectively.[5-7] The binding energy of Co at Vo-CCO NWs shift slightly toward lower energy, which is due to the presence of oxygen vacancy.[8] The C 1s peaks (**Fig. S11B**) around 289.2 eV of carboxyl carbons shift to higher binding energy, which is consistent with the result of slight shift towards lower energy for Co XPS spectra.[9, 10]

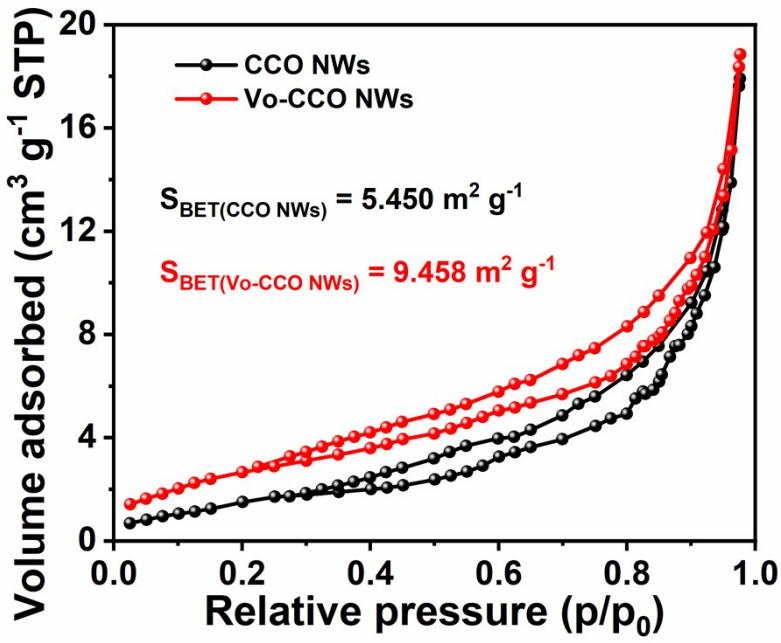

Fig. S12. N_2 adsorption-desorption isotherm of CCO NWs and Vo-CCO NWs.

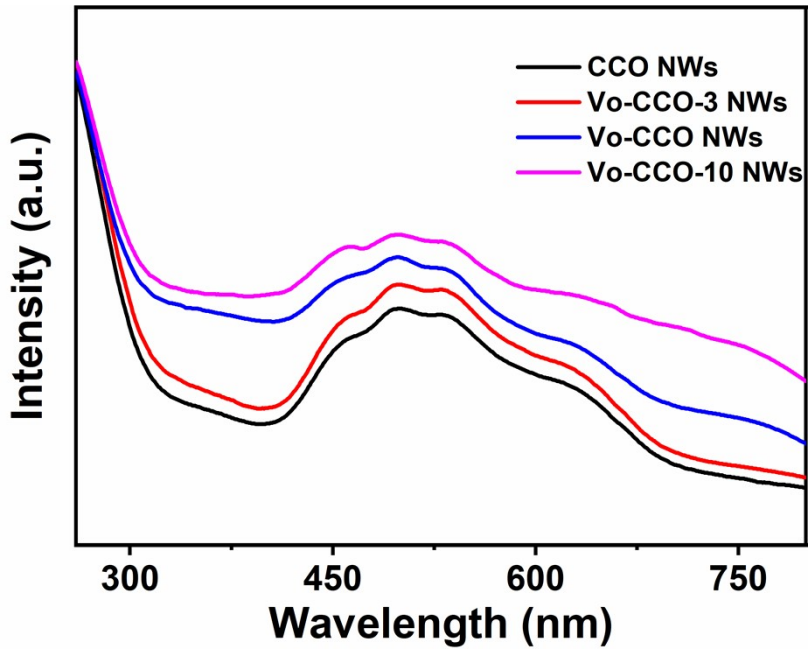

Fig. S13. UV-Vis DRS of as-prepared different samples.

The optical response behavior of as-prepared photocatalysts was determined by UV-Vis diffuse reflectance spectra (DRS). All of as-prepared photocatalysts reveal multiband characteristics with a main optical absorption in the region below 400 nm. The second optical absorption in the visible region at the center of *ca.* 500 nm may be due to d-d transitions of Co atoms. [7, 11, 12]

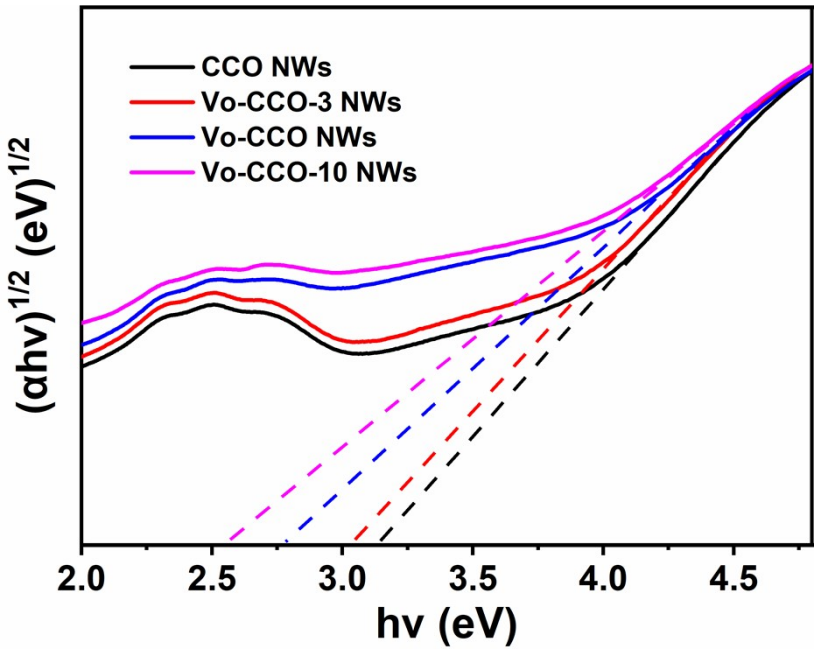

Fig. S14. The band gap of as-prepared different samples calculated by using $(\alpha h\nu)^2$ vs. *hv* for Tauc plots.

The band gap of CCO NWs, Vo-CCO-3 NWs, Vo-CCO NWs and Vo-CCO-10 NWs were calculated as 3.13, 3.03, 2.78 and 2.56 eV, respectively.

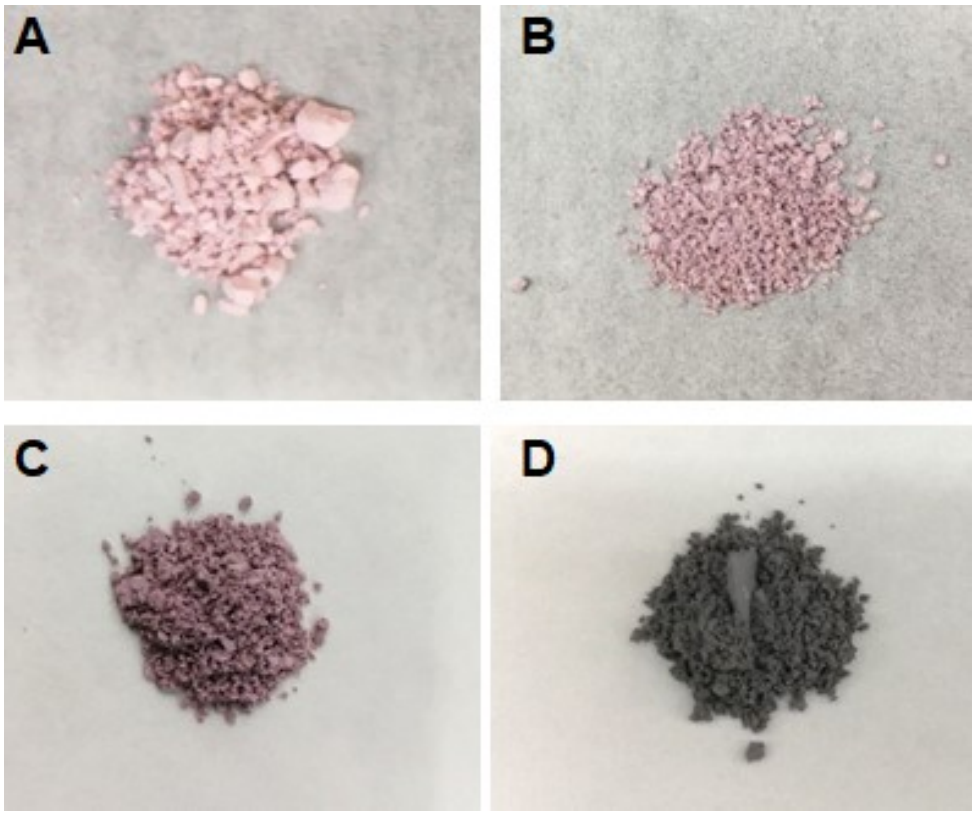

Fig. S15. The photograph of as-prepared CCO NWs photocatalyst with different illumination time. (A) 0 h, (B) 3 h, (C) 5 h, (D) 10 h.

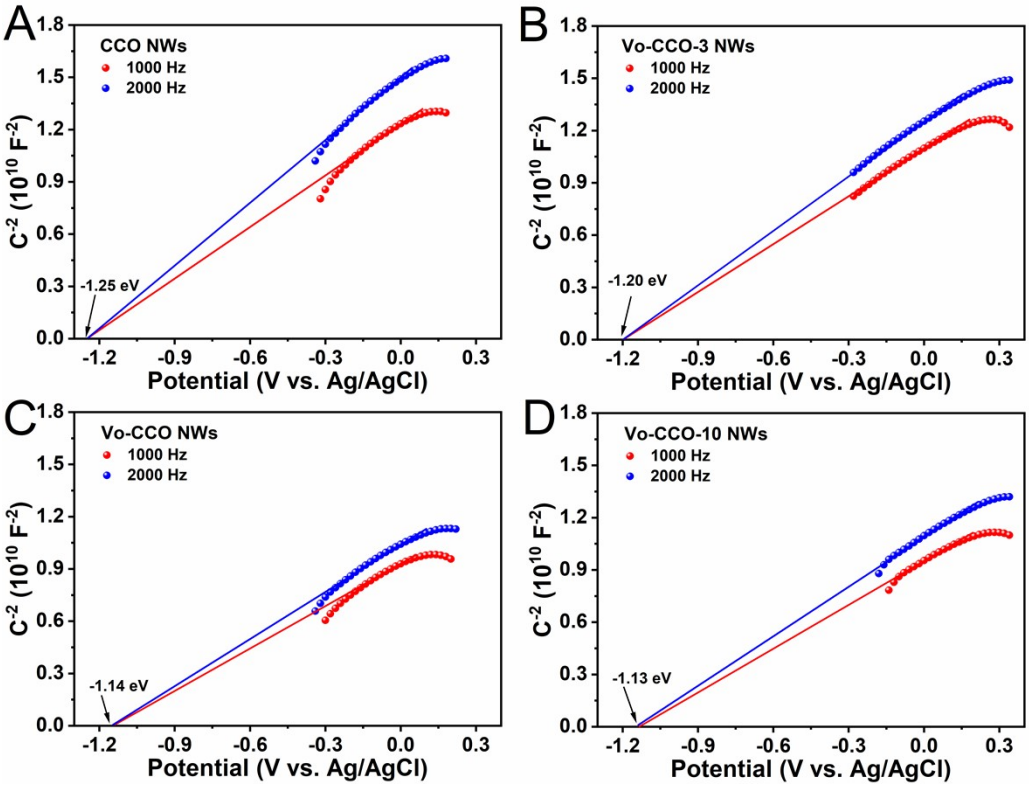

Fig. S16. Mott−Schottky plots of the as-prepared (A) CCO NWs, (B) Vo-CCO-3 NWs, (C) Vo-CCO NWs and (D) Vo-CCO-10 NWs.

The flat-band potentials were measured by the means of Mott-Schottky plots measurement. The positive slope of the Mott-Schottky plots for the CCO samples indicated the n-type nature. And the V_{fb} is located just below the bottom of conduction band (CB) (about 0.1 eV) for an n-type semiconductor.[13, 14] Therefore, the CB of CCO NWs, Vo-CCO-3 NWs, Vo-CCO NWs and Vo-CCO-10 are -1.35, -1.30, -1.24 and -1.23 V *vs.* Ag/AgCl electrode (-0.74, -0.69, -0.63 and -0.62 V *vs.* NHE, normal hydrogen electrode, pH = 7), respectively.

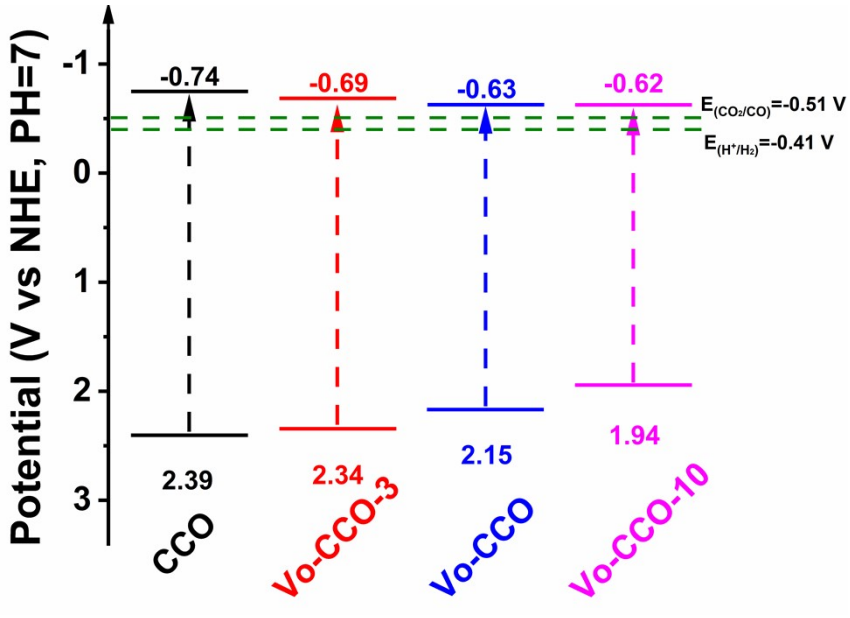

Fig. S17. Electronic band structures of as-prepared samples with different samples.

The CB of all prepared catalysts are more negative than the reduction potentials of $E(CO_2/CO)$ (-0.51 V *vs.* NHE, pH = 7),[15, 16] which indicated that CCO NWs and Vo-CCO NWs can reduce CO_2 to CO product.

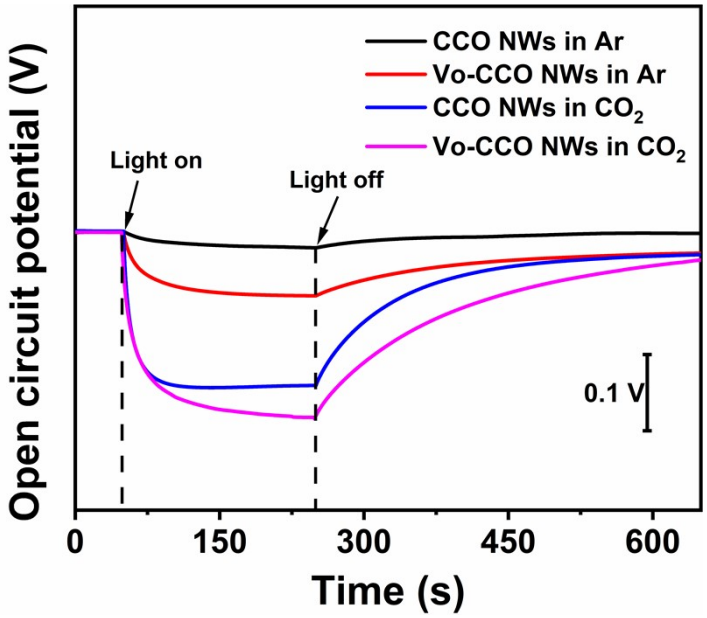

Fig. S18. Open circuit potential curves of the CCO and Vo-CCO NWs (0.5 M Na_2SO_4 with saturated Ar or CO_2, respectively).

The open circuit potential (Voc) was measured under the same condition with photocurrent curves. As indicated in **Fig. S18**, the Vo-CCO NWs at CO_2-saturated solution attain maximal photovoltage when the light is on, indicating that Vo on the surface of Vo-CCO NWs have the strongest electron transfer capability. Furthermore, the Voc for Vo-CCO NWs exhibits a longer time to reach the baseline than the pristine CCO when the light is turned off, which demonstrate that the Vo is effective for accelerating the charge separation and hindering the photocarriers recombination.[13] The Vo can provide more active sites and increase the CO_2 adsorption energy, which makes CO_2 molecules more easily adsorbed and activated on the surface of photocatalyst.[16] Moreover, the defect energy level caused by Vo may overwhelm the recombination of e^--h^+ pairs, change the transfer path and prolong the life of photocarriers. [17, 18] Therefore, a slower photovoltage decay behavior is displayed when the light is turned off. The Voc results are consistent with the results of photocurrent curves.[13]

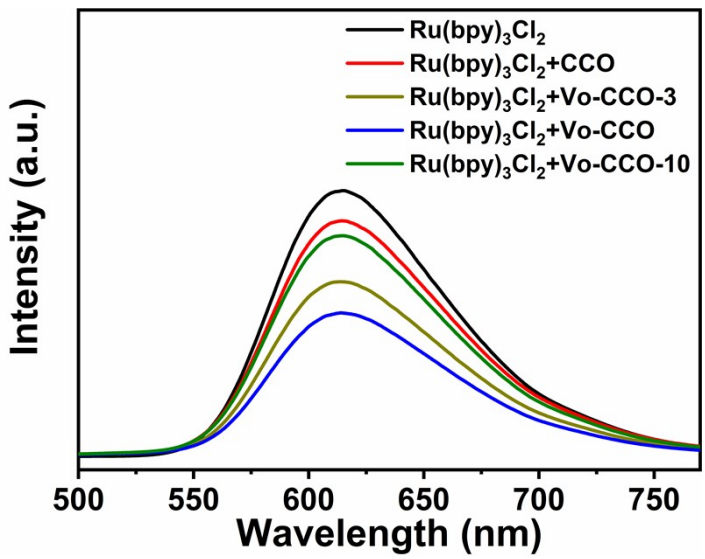

Fig. S19. Steady-state PL spectra of as-prepared different samples (λ_{ex} = 400 nm).

The steady-state PL spectroscopy is employed to understand the carrier recombination process. The $[Ru(bpy)_3]Cl_2$ with an excitation wavelength of 400 nm shows a strong emission peak in the region centered at around 610 nm.[19, 20] The $[Ru(bpy)_3]Cl_2$ exhibits the highest PL intensity due to the stronger radiative recombination behavior. With the addition of CCO NWs series materials, the PL of the excited $[Ru(bpy)_3]Cl_2$ is gradually quenched and $[Ru(bpy)_3]Cl_2$ + Vo-CCO NWs show the lowest PL intensity, which confirms that the quenching of PL intensity should be directly caused by the transfer of photoexcited electrons from $[Ru(bpy)_3]Cl_2$ to as-prepared photocatalysts and Vo-CCO NWs have the strongest electron transfer capability. However, the superfluous Vo is generated when prolong self-photoetching time to 10 h (Vo-CCO-10 NWs). The superfluous Vo is detrimental to the separation of photogenerated e^--h^+ pairs, which can be verified by stronger PL emission peak of $[Ru(bpy)_3]Cl_2$ + Vo-CCO-10 NWs than $[Ru(bpy)_3]Cl_2$ + Vo-CCO NWs.

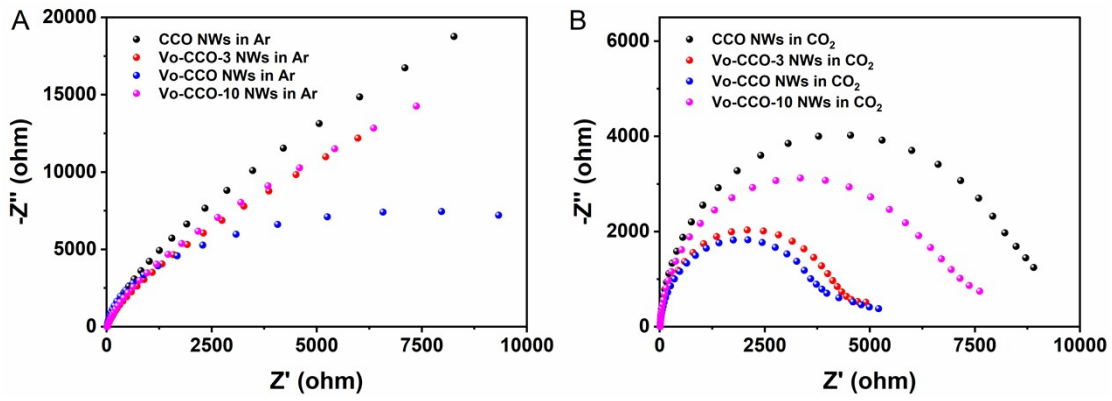

Fig. S20. Electrochemical impedance spectra of the as-prepared products under light illumination in the (A) Ar and (B) CO_2 saturated 0.5 M Na_2SO_4 solution, respectively.

The arc radius of Nyquist plots in the electrochemical impedance spectra (EIS) are shown in **Fig. S20**. The Vo-CCO NWs expose smallest arc radius of Nyquist plots in Ar and CO_2-saturated Na_2SO_4 solution, respectively, indicating a larger separation rate of the photoinduced electron-hole pairs for Vo-CCO NWs than other CCO series materials.[14] What's more, EIS of CCO series materials in CO_2-saturated Na_2SO_4 solution is smaller than that in Ar, which means that CCO series materials can willingly facilitate the capture and activation of CO_2 molecules.[16] However, the superfluous Vo of Vo-CCO-10 NWs induces the recombination of electrons and holes, which can be verified by enlarged arc radius than Vo-CCO NWs in Nyquist plots at EIS.

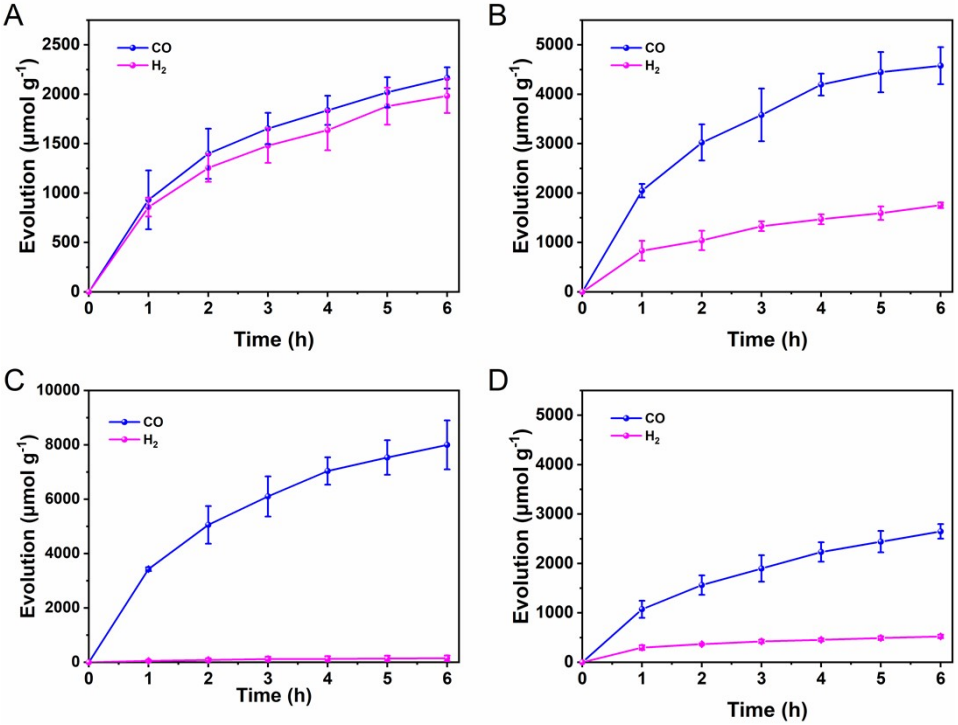

Fig. S21. CO_2 photoreduction activities of (A) CCO NWs, (B)Vo-CCO-3 NWs, (C) Vo-CCO NWs and (D) Vo-CCO-10 NWs.

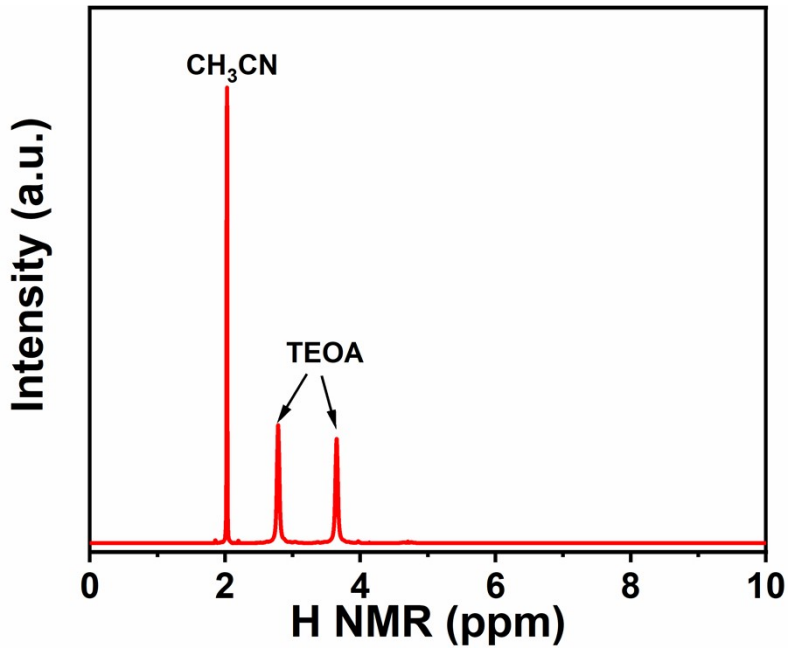

Fig. S22. ^{1}H-NMR spectra of the liquid phase taken from the reaction system of Vo-CCO NWs after photocatalytic CO_2 reduction test.

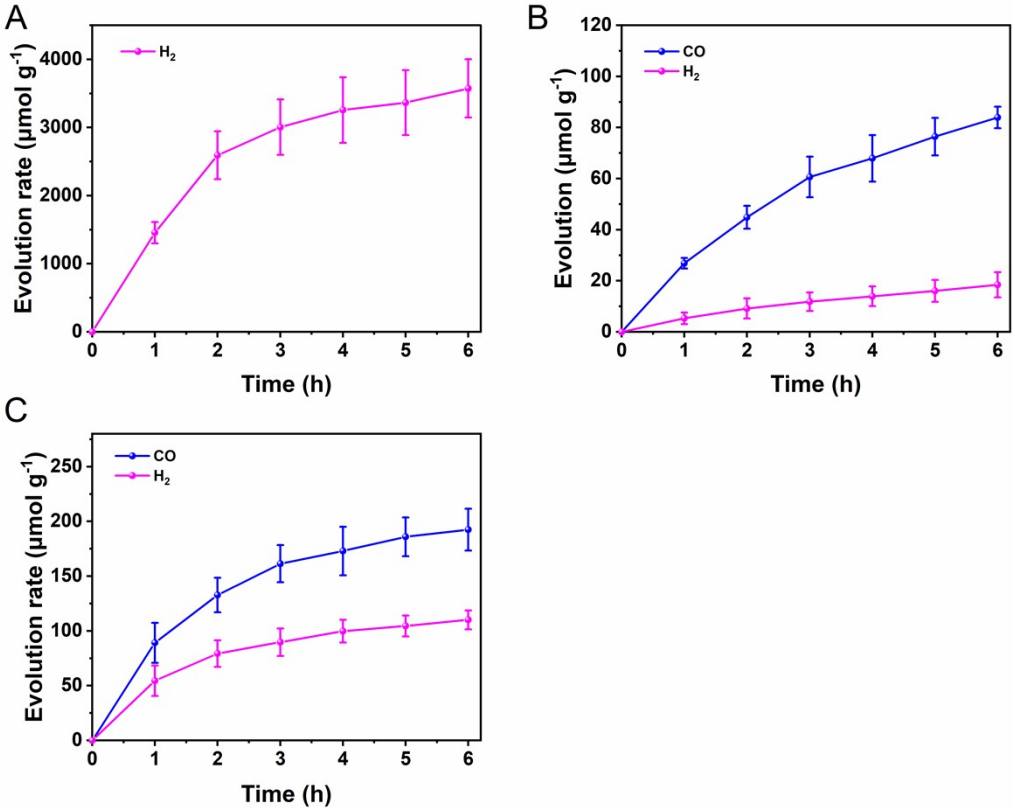

Fig. S23. Photocatalytic CO_2 reduction performance under various conditions: (A) using Ar to replace CO_2; (B) without $Ru(bpy)_3Cl_2$; (C) without Vo-CCO NWs.

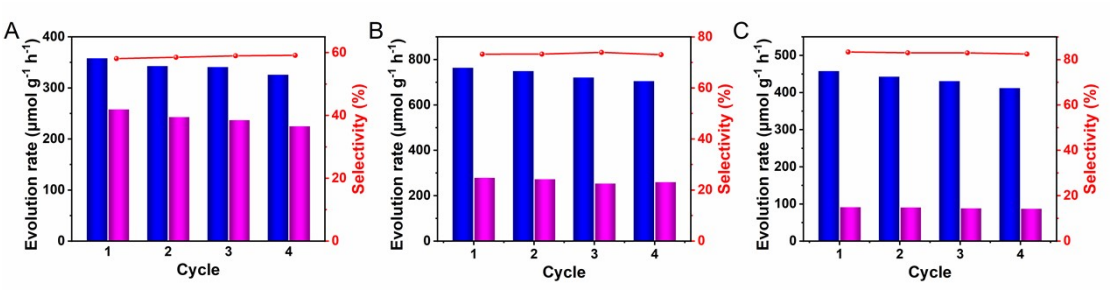

Fig. S24. Stability test of (A) CCO, (B) Vo-CCO-3 and (C) Vo-CCO-10 NWs, respcetively.

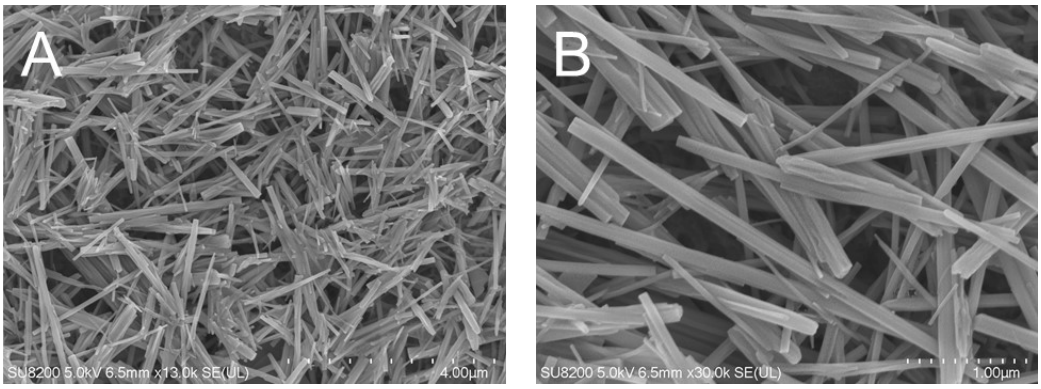

Fig. S25. SEM images of the as-prepared Vo-CCO NWs after durability test.

The morphology of Vo-CCO NWs does not exhibit obvious change by SEM images, demonstrating good durability of Vo-CCO NWs.

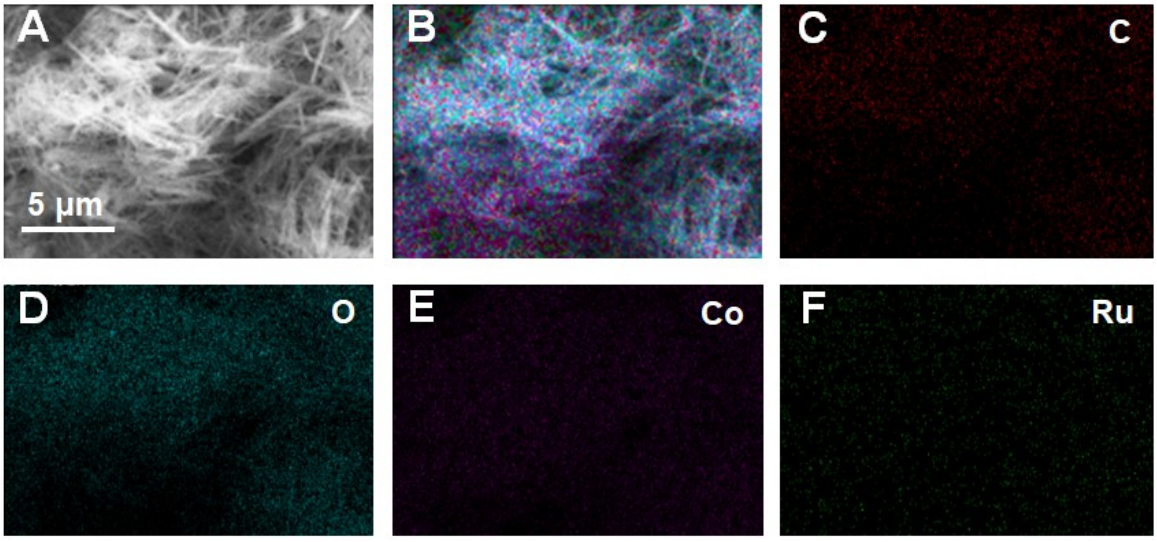

Fig. S26. SEM image elemental mapping of the as-prepared Vo-CCO NWs after durability test.

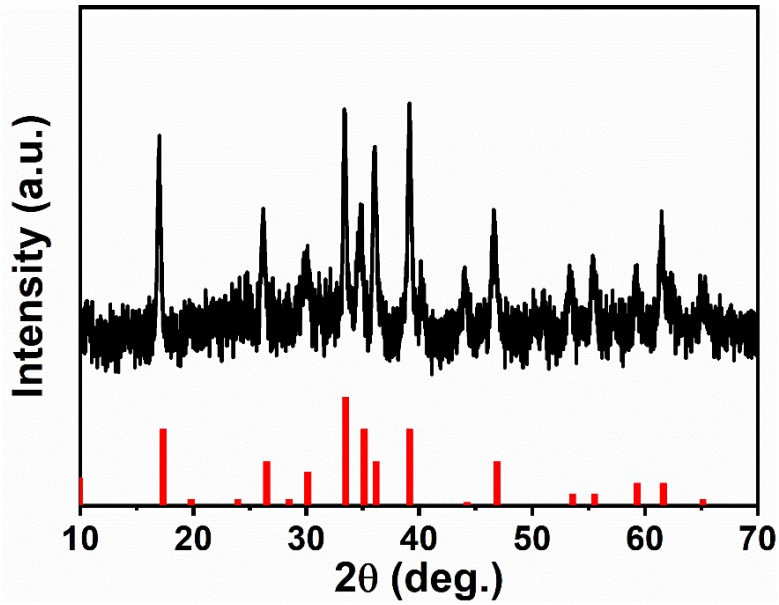

Fig. S27. XRD patterns of the as-prepared Vo-CCO NWs after durability test.

The structure of Vo-CCO does not exhibit obvious change by XRD patterns after 4 cycles (24 h), demonstrating good durability of Vo-CCO.

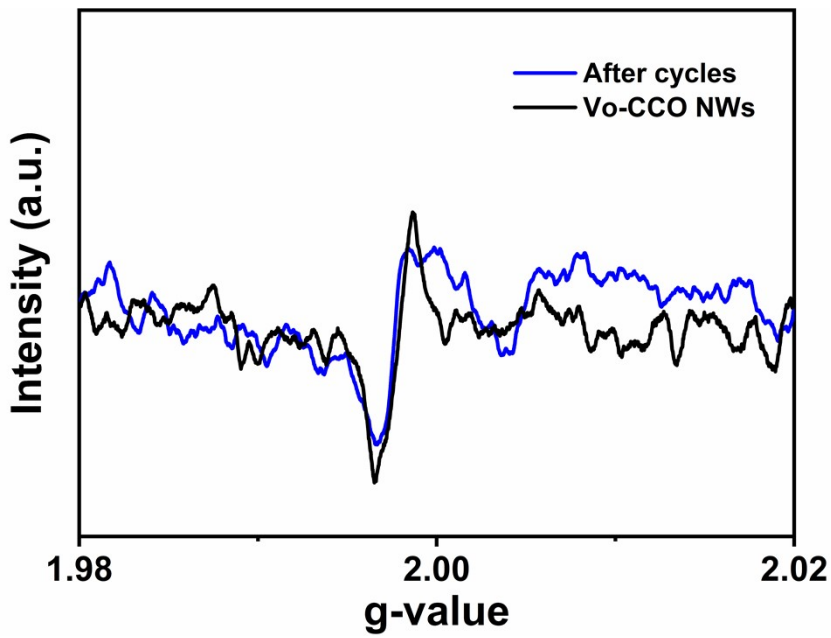

Fig. S28. EPR spectra of Vo-CCO NWS before and after cycles.

The EPR spectrum after stability tests were characterized and shown in **Fig. S28.** The EPR signal of Vo-CCO NWs after cycles are weaker than fresh one. The reduced EPR signal may be the shelter of adsorbed CO_2 and intermediate species of CO_2 reduction, which can be demonstrated by XPS spectra of Vo-CCO NWs after cycles.

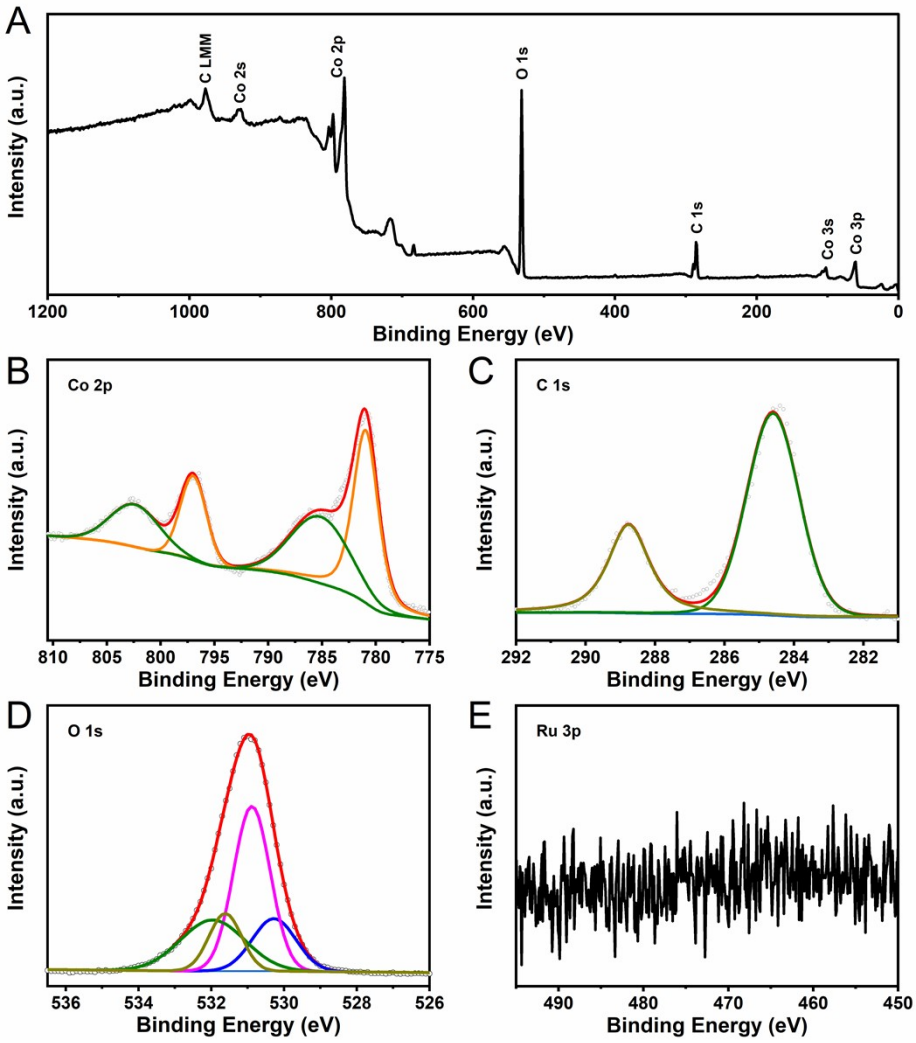

Fig. S29. XPS spectra of Vo-CCO NWs after cycle test.

The XPS spectra after cycles of Vo-CCO NWs were presented in **Fig. S29.** The peaks at 797.0 and 780.9 eV of Co are attributed to Co $2p_{1/2}$ and $2p_{3/2}$ spin-orbit of Co^{2+}, respectively.[5-7] Compared with Vo-CCO NWs, the Co 2p, C 1s and O 1s spectra shift slightly toward the lower binding energy, which is due to the marginal adsorption of photosensitizer and intermediate species of CO_2 reduction. The increased relative ratios of C=O group at 288.8 eV of the C 1s spectra compared with pristine Vo-CCO NWs may be the adsorption of intermediate species of CO_2 reduction.[21] The result can also be observed in the increased relative ratios of C=O in O 1s spectrum at 530.5 eV. [21-24] The peak of Vo reduce slightly is in keeping with EPR results.

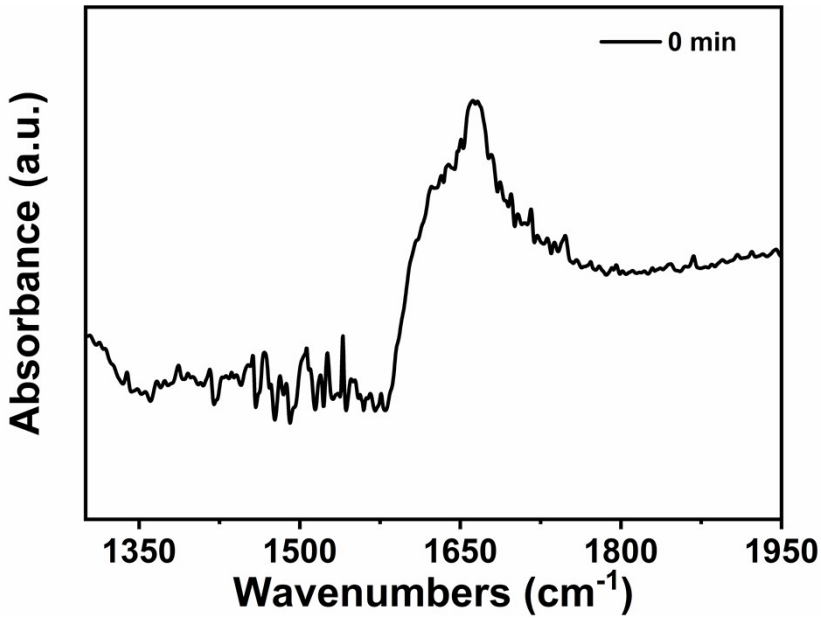

Fig. S30. The in-situ FTIR curve of Vo-CCO NWs in 0 minutes.

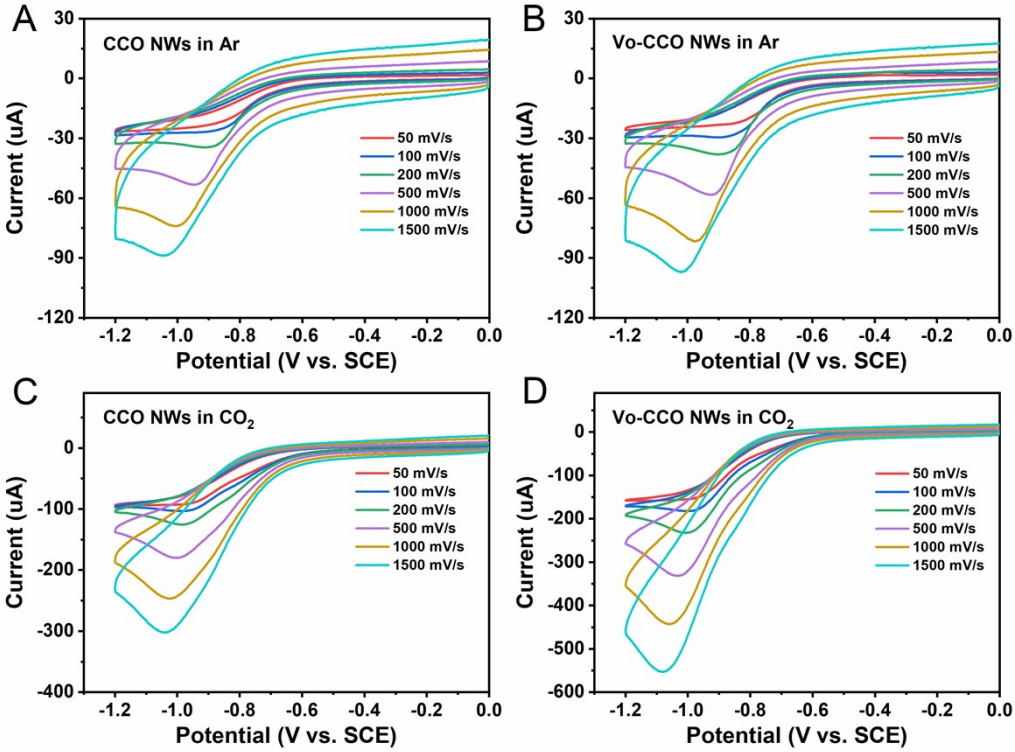

Fig. S31. CV curves of CCO and Vo-CCO NWs in CH_3CN containing 0.1 M $TBAPF_6$ as a supporting electrolyte under Ar or CO_2 atmosphere with different scan rate, respectively.

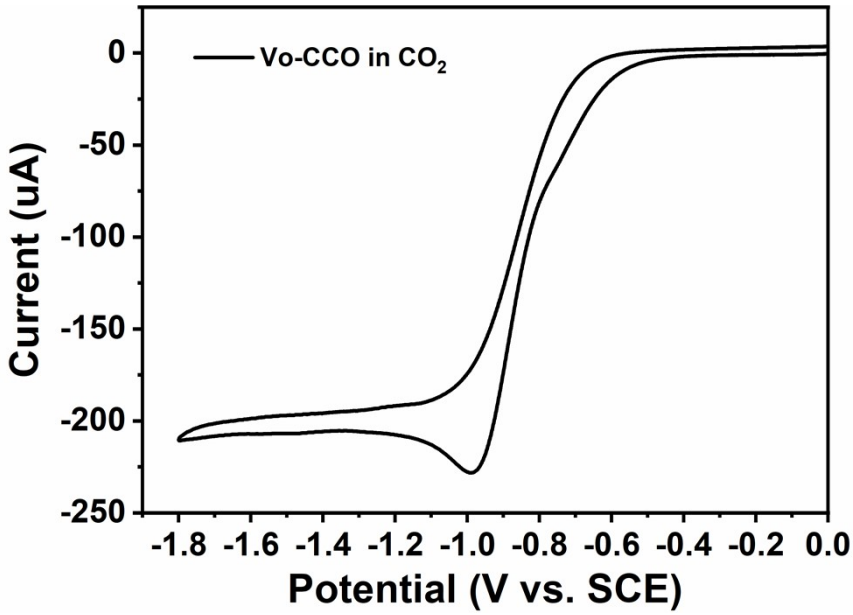

Fig. S32. CV curve in CH_3CN containing 0.1 M $TBAPF_6$ as a supporting electrolyte under CO_2 atmosphere with scan rate at 200 mV/s.

Table S1. Relative ratio of CO_3^{2-}, Co-O, Vo and H_2O determined by O 1s XPS spectra.

Samples	CO_3^{2-} (%)	Co-O (%)	Vo (%)	H_2O (%)
CCO NWs	55.26	17.87	6.38	20.49
CCO NWs After Ar^+ etching	56.93	17.11	6.36	19.60
Vo-CCO NWs	49.93	13.39	17.01	19.67
Vo-CCO NWs After Ar^+ etching	54.38	16.75	8.90	19.97
After cycles	44.78	16.94	13.90	24.38

Table S2. The atomic ratio of CCO and Vo-CCO NWs before and after Ar^+ etching based on the XPS data, respectively.

Samples	C (%)	O (%)	Co (%)	Co/O (%)
CCO NWs	39.63	46.03	14.34	31.15
CCO NWs After Ar^+ etching	38.56	46.86	14.58	31.11
Vo-CCO NWs	38.48	46.30	15.22	32.87
Vo-CCO NWs After Ar^+ etching	37.57	47.58	14.85	31.21

Table S3. FT-EXAFS fitting parameters at the Co K-edge for CCO and Vo-CCO NWs（S_0^2=0.776）

Sample	Shell	*CN*[a]	*R*(Å)[b]	$\sigma^2\times10^3$(Å^2)[c]	ΔE_0 (eV)[d]	*R* factor
CCO NWs	Co-O	6.2±0.7	2.05±0.1	8.2±1.5	-2.4±1.2	0.009
	Co-Co	5.7±2.1	3.12±0.02	15.2±4.0	-2.0±2.8	
Vo-CCO NWs	Co-O	5.2±1.1	2.06±0.02	6.9±3.3	-2.9±1.9	0.018
	Co-Co	7.9±6.7	3.13±0.06	22.6±11.5	-1.7±4.9	

[a]*CN*: coordination numbers; [b]*R*: bond distance; [c]σ^2: Debye-Waller factors; [d]ΔE_0: the inner potential correction. *R* factor: goodness of fit.

Table S4. Band gap, VB and CB energy level (vs. NHE, pH=7) of as-prepared samples calculated on the basis of UV-vis DRS and Mott-Schottky plots.

Photocatalysts	Band-gap(eV)	Mott-Schottky	
		VB(eV)	CB(eV)
CCO NWs	3.13	2.39	-0.74
Vo-CCO-3 NWs	3.03	2.34	-0.69
Vo-CCO NWs	2.78	2.15	-0.63
Vo-CCO-10 NWs	2.56	1.94	-0.62

Table S5. Photocatalytic CO_2 reduction performance of as-prepared photocatalysts under various conditions.

Catalysts	Photosensitizer	Reaction medium	Light source	Product rate ($\mu mol\ h^{-1}\ g^{-1}$)	Selectivity
CCO NWs	$[Ru(bpy)_3]Cl_2$	MeCN/ H_2O/ TEOA	300 W Xe lamp (λ > 420 nm)	CO: 343.85 H_2: 302.08	53.2% 46.8%
Vo-CCO-3 NWs	$[Ru(bpy)_3]Cl_2$	MeCN/ H_2O/ TEOA	300 W Xe lamp (λ > 420 nm)	CO: 763.07 H_2: 279.81	73.2% 26.8%
Vo-CCO NWs	$[Ru(bpy)_3]Cl_2$	MeCN/ H_2O/ TEOA	300 W Xe lamp (λ > 420 nm)	CO: 1333.20 H_2: 25.12	98.2% 1.8 %
Vo-CCO-10 NWs	$[Ru(bpy)_3]Cl_2$	MeCN/ H_2O/ TEOA	300 W Xe lamp (λ > 420 nm)	CO: 441.62 H_2: 87.37	83.5% 16.5%
Vo-CCO NWs	--	MeCN/ H_2O/ TEOA	300 W Xe lamp (λ > 420 nm)	CO: 14.93 H_2: 3.30	81.9% 18.1%
Vo-CCO NWs	$[Ru(bpy)_3]Cl_2$	MeCN/ H_2O	300 W Xe lamp (λ > 420 nm)	n.d.	--
Vo-CCO NWs	$[Ru(bpy)_3]Cl_2$	MeCN/ H_2O/ TEOA	--	n.d.	--
Vo-CCO NWs (with saturated Ar)	$[Ru(bpy)_3]Cl_2$	MeCN/ H_2O/ TEOA	300 W Xe lamp (λ > 420 nm)	H_2: 620.45	--
--	$[Ru(bpy)_3]Cl_2$	MeCN/ H_2O/ TEOA	300 W Xe lamp (λ > 420 nm)	CO: 36.64 H_2: 19.46	65.3% 34.7%

Table S6. Summary of the photocatalytic CO evolution performance of some cobalt based catalysts.

Catalysts	Photosensitizer	Reaction medium	Light source	Product rate ($\mu mol\ h^{-1}\ g^{-1}$)/ Selectivity	Ref.
Vo-CCO NWs	$[Ru(bpy)_3]Cl_2$	MeCN/ H_2O/ TEOA	300 W Xe lamp (λ > 420 nm)	CO: 1333.20/ 98.2% H_2: 25.12/ 1.8 %	**This work**
Co-G nanosheets	$[Ru(bpy)_3]Cl_2$	MeCN/ H_2O/ TEOA	300 W Xe lamp (λ > 420 nm)	CO: --/ 79.4% H_2: --/20.6%	20
CoMOL@GO	$Ru(phen)_3(PF_6)_3$	MeCN/ H_2O/ TEOA	100 mW cm^{-2} (λ = 450 nm)	CO: 1801.7/ 95% H_2: 94.8/ 5 %	25
2D-Co_2TCPE	$[Ru(bpy)_3]Cl_2$	MeCN/ H_2O/ TEOA	300 W Xe lamp (800>λ > 420 nm)	CO: 2560 / 75.8% H_2: 200/ 24.2%	26
Au_c-C-Co	--	H_2O/ TEOA	300 W Xe lamp (λ > 420 nm)	CH_4: 0.075/ 5.7% CO: 3.451/ 65.2% H_2: 1.539/ 29.1%	27
$(Co/Ru)_{2.4}$-UiO-67(bpydc)	--	MeCN/ H_2O/ TEOA	450nm LED lamp	CO: 282.5/ 33.1% H_2: 570.1/ 66.9%	28
PMMCoCC1200	$[Ru(bpy)_3]Cl_2$	MeCN/ H_2O/ TEOA	300 W Xe lamp (λ > 420 nm)	CO: 448/ 64.21% H_2: 250/ 35.79%	29
Co^{2+}@ C_3N_4	--	MeCN/ TEOA	300 W Xe lamp (λ > 420 nm)	CO: 528/ 83.5% H_2: 104/ 16.5%	30
Co_3O_4 hexagonal platelets	$[Ru(bpy)_3]Cl_2$	MeCN/ H_2O/ TEOA	300 W Xe lamp (λ > 420 nm)	CO: 2003/ 77.1% H_2: 595/ 22.9%	31

CoAl-LDH nanosheets	--	H_2O	500 W Xe lamp	CH_4: 77% CO: 7% H_2: 16%	32
MOF-525-Co	--	MeCN/ TEOA	300 W Xe lamp (800＞λ> 400 nm)	CH_4: 36.67/ 15.5% CO: 201.6/ 84.5%	33
QS-Co_3O_4 HoMSs (ZIF-67)	--	H_2O	AM 1.5G	CO: 46.3/--	34
Mpg-CNx| $CoPPc_{11.9}$	--	MeCN/ TEOA	300 W Xe lamp (λ > 300 nm)	CO: 20.85/ 84.7% H_2: 3.79/ 15.3%	35
CoO-Mo8	$[Ru(bpy)_3]Cl_2$	MeCN/ H_2O/ TEOA	300 W Xe lamp (λ > 400 nm)	CO: 4165/ 26.5% H_2: 11555/ 73.5%	36
COF-367-Co NSs	$[Ru(bpy)_3]Cl_2$	$KHCO_3$/H_2O/ AA	300 W Xe lamp (λ > 420 nm)	CO: 10162/ 78.0% H_2: 2875/ 22.0%	37

REFERRENCE:

1. B. Ravel and M. Newville, *J Synchrotron Radiat*, 2005, **12**, 537-541.
2. Y. Wang, S. Wang, S. L. Zhang and X. W. Lou, *Angew. Chem. Int. Ed.*, 2020, **59**, 11918-11922.
3. Z. Liu, R. Ma, M. Osada, K. Takada and T. Sasaki, *J. Am. Chem. Soc.*, 2005, **127**, 13869-13874.
4. L. Zhu, Z. Wen, W. Mei, Y. Li and Z. Ye, *J. Phys. Chem. C*, 2013, **117**, 20465-20473.
5. Q. Qian, Y. Li, Y. Liu and G. Zhang, *Appl. Catal. B*, 2020, **266**, 118642.
6. Y. Liu, J. Zhang, Y. Li, Q. Qian, Z. Li, Y. Zhu and G. Zhang, *Nat. Commun.*, 2020, **11**, 1853.
7. B. He, H. Liu, Z. Lin, L. Yan, J. Ning, Y. Zhong, C. Zheng, Z. Zhang and Y. Hu, *Chem. Eng. J.*, 2019, **359**, 924-932.
8. S. Sun, M. Watanabe, J. Wu, Q. An and T. Ishihara, *J. Am. Chem. Soc.*, 2018, **140**, 6474-6482.
9. D. Ferrah, A. R. Haines, R. P. Galhenage, J. P. Bruce, A. D. Babore, A. Hunt, I. Waluyo and J. C. Hemminger, *ACS Catal.*, 2019, **9**, 6783-6802.
10. Y. Zhang, A. Savara and D. R. Mullins, *J. Phys. Chem. C*, 2017, **121**, 23436-23445.
11. L. Wang, Y. Zhang, X. Gu, Y. Zhang and H. Su, *Catal. Sci. Technol.*, 2018, **8**, 601-610.
12. J. Di, C. Chen, S. Z. Yang, S. Chen, M. Duan, J. Xiong, C. Zhu, R. Long, W. Hao, Z. Chi, H. Chen, Y. X. Weng, J. Xia, L. Song, S. Li, H. Li and Z. Liu, *Nat. Commun.*, 2019, **10**, 2840.
13. H. Liu, K. Tian, J. Ning, Y. Zhong, Z. Zhang and Y. Hu, *ACS Catal.*, 2019, **9**, 1211-1219.
14. H. H. Liu, L. Li, C. F. Guo, J. Q. Ning, Y. J. Zhong and Y. Hu, *Chem. Eng. J.*, 2020, **385**, 123929.
15. Y. Zhao, G. I. N. Waterhouse, G. Chen, X. Xiong, L. Z. Wu, C. H. Tung and T. Zhang, *Chem. Soc. Rev.*, 2019, **48**, 1972-2010.
16. X. Chang, T. Wang and J. Gong, *Energy Environ. Sci.*, 2016, **9**, 2177-2196.
17. Z. Geng, X. Kong, W. Chen, H. Su, Y. Liu, F. Cai, G. Wang and J. Zeng, *Angew. Chem. Int. Ed.*, 2018, **57**, 6054-6059.
18. M. Wang, M. Shen, X. Jin, J. Tian, M. Li, Y. Zhou, L. Zhang, Y. Li and J. Shi, *ACS Catal.*, 2019, **9**, 4573-4581.
19. Z. Wang, J. Yang, J. Cao, W. Chen, G. Wang, F. Liao, X. Zhou, F. Zhou, R. Li, Z. Q. Yu, G. Zhang, X. Duan and Y. Wu, *ACS Nano*, 2020, **14**, 6164-6172.
20. C. Gao, S. Chen, Y. Wang, J. Wang, X. Zheng, J. Zhu, L. Song, W. Zhang and Y. Xiong, *Adv. Mater.*, 2018, **30**, 1704624.
21. Z.-W. Huang, Z.-J. Li, Q.-Y. Wu, L.-R. Zheng, L.-M. Zhou, Z.-F. Chai, X.-L. Wang and W.-Q. Shi, *Environ. Sci.: Nano*, 2018, **5**, 2077-2087.
22. W. Wei, S. Cui, L. Ding, L. Mi, W. Chen and X. Hu, *ACS Appl. Mater. Interfaces*, 2017, **9**, 40655-40670.
23. H. Yu, J. Li, Y. Zhang, S. Yang, K. Han, F. Dong, T. Ma and H. Huang, *Angew. Chem. Int. Ed.*, 2019, **58**, 3880-3884.
24. X. Wang, L. Lu, B. Wang, Z. Xu, Z. Xin, S. Yan, Z. Geng and Z. Zou, *Adv. Funct. Mater.*, 2018, **28**, 1804191.
25. J. W. Wang, L. Z. Qiao, H. D. Nie, H. H. Huang, Y. Li, S. Yao, M. Liu, Z. M. Zhang, Z. H. Kang and T. B. Lu, *Nat. Commun.*, 2021, **12**, 813.

26. H. L. Zheng, S. L. Huang, M. B. Luo, Q. Wei, E. X. Chen, L. He and Q. Lin, *Angew. Chem. Int. Ed.*, 2020, **59**, 23588-23592.
27. X. Cui, J. Wang, B. Liu, S. Ling, R. Long and Y. Xiong, *J. Am. Chem. Soc.*, 2018, **140**, 16514-16520.
28. M. Liu, Y.-F. Mu, S. Yao, S. Guo, X.-W. Guo, Z.-M. Zhang and T.-B. Lu, *Appl. Catal. B*, 2019, **245**, 496-501.
29. K. Zhao, S. Zhao, C. Gao, J. Qi, H. Yin, D. Wei, M. F. Mideksa, X. Wang, Y. Gao and Z. Tang, *Small*, 2018, **14**, 1800762.
30. P. Huang, J. Huang, S. A. Pantovich, A. D. Carl, T. G. Fenton, C. A. Caputo, R. L. Grimm, A. I. Frenkel and G. Li, *J. Am. Chem. Soc.*, 2018, **140**, 16042-16047.
31. C. Gao, Q. Meng, K. Zhao, H. Yin, D. Wang, J. Guo, S. Zhao, L. Chang, M. He and Q. Li, *Adv. Mater.*, 2016, **28**, 6485-6490.
32. K. Wang, L. Zhang, Y. Su, D. Shao, S. Zeng and W. Wang, *J. Mater. Chem. A*, 2018, **6**, 8366-8373.
33. H. Zhang, J. Wei, J. Dong, G. Liu, L. Shi, P. An, G. Zhao, J. Kong, X. Wang, X. Meng, J. Zhang and J. Ye, *Angew. Chem.*, 2016, **128**, 14522-14526.
34. L. Wang, J. Wan, Y. Zhao, N. Yang and D. Wang, *J. Am. Chem. Soc.*, 2019, **141**, 2238-2241.
35. S. Roy and E. Reisner, *Angew. Chem. Int. Ed.*, 2019, **58**, 12180-12184.
36. H. Yang, D. Yang and X. Wang, *Angew. Chem. Int. Ed.*, 2020, **59**, 15527-15531.
37. W. Liu, X. Li, C. Wang, H. Pan, W. Liu, K. Wang, Q. Zeng, R. Wang and J. Jiang, *J. Am. Chem. Soc.*, 2019, **141**, 17431-17440.